Investigation of Galileo Probe Entry Heating with Coupled Radiation and Ablation

Aaron J. Erb,* Thomas K. West, † and Christopher O. Johnston ‡
NASA Langley Research Center, Hampton, VA 23681

This paper presents a trajectory-based heating and ablation study of the Galileo Probe forebody flow and thermal protection system performance. The validity of modeling assumptions regarding diffusion, radiative heating, and ablation made in previous work, including pre-flight predictions, are addressed. The Navier-Stokes equations are solved assuming a one temperature chemical nonequilibrium flowfield with coupled radiation and ablation. Geometric changes in the forebody due to ablation are accounted for. Solving the Stefan-Maxwell equations to compute the species mass diffusion in the flowfield, instead of assuming a constant Schmidt number as was done in previous studies, was found to significantly increase total predicted recession by about 10% on the flank, due to increased convective heating. Application of the high-fidelity ray-tracing approach resulted in a 10% reduction in the radiative heating along the forebody when compared to the heritage tangent-slab approximation. Other modeling approaches, such as state-specific H modeling, application of ray-tracing for coupled flowfield radiative source terms, and including precursor absorption were found to have a minimal impact on recession. The resulting nominal prediction was found to be nearly within the uncertainty of the flight data along the entire surface of the probe. This improved agreement relative to past studies is due to the notable impact of shape change, multicomponent diffusion, and ray-tracing radiative heating, most of which were not included in previous models. To provide uncertainty bounds for the present simulations, an uncertainty analysis was performed. Sources of uncertainty were identified in the ablation modeling, radiation modeling, flowfield kinetics, turbulence modeling, and thermodynamic properties of select species. The combined impact of the uncertainties resulted in -13%, +17% uncertainty in stagnation point recession and a near constant ±0.35 cm uncertainty on the flank.

*Pathways Intern, Vehicle Analysis Branch, Systems Analysis and Concepts Directorate, Student Member AIAA.
†Aerospace Engineer, Vehicle Analysis Branch, Systems Analysis and Concepts Directorate, Member AIAA.
‡Aerospace Engineer, Aerothermodynamics Branch, Research Directorate, AIAA Associate Fellow.

Nomenclature

h	enthalpy (J/kg-K)
$\dot{m}$	mass injection rate (kg/m^2-s)
q_c	convective heating (W/cm^2)
q_{cond}	heat conduction (W/cm^2)
q_{rad}	radiative heating (W/cm^2)
R_n	effective nose radius (cm)
S	distance along vehicle surface (cm)
Δs	surface recession (cm)
T	temperature (K)
α	thermal diffusivity (m^2/s)
ϵ	surface emissivity
ρ	density (kg/m^3)
σ	Stefan-Boltzmann constant (W/m^2-K^4)

subscripts

c	char material
g	pyrolysis gas
i	grid point along surface
v	virgin material
w	wall property

I. Introduction

On 7 December 1995, the Galileo Probe deceleration module entered Jupiter's atmosphere, experiencing the most severe atmospheric entry conditions ever encountered by a planetary entry vehicle. It descended into the Jovian atmosphere with a relative velocity of 47.4 km/s. Throughout the 250 g_e deceleration phase from Mach 50, the Galileo forebody carbon phenolic heatshield experienced a peak heating rate of 30 kW/cm^2 and a heat load of 300 kJ/cm^2. The cross section of the Galileo probe [1–3] is shown in Fig. 1a.

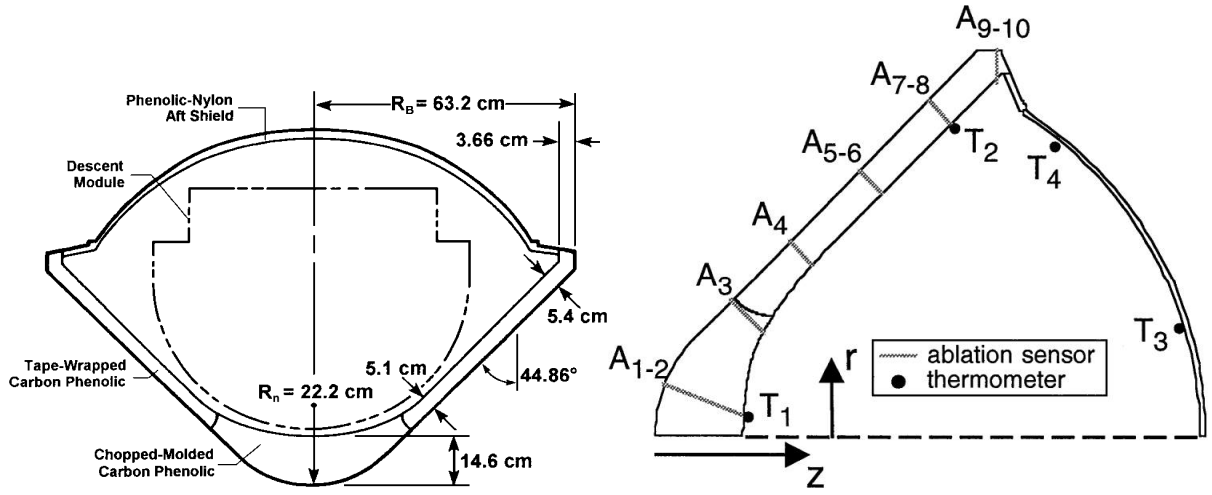

(a) Cross section of Galileo probe deceleration module [1–3].

(b) Ablation sensor locations installed in Galileo probe[2, 3].

Fig. 1 Galileo probe deceleration module overview [2].

The forebody shape was an axisymmetric sphere-cone with a 22.2 cm nose radius and a 44.86 degree half angle frustum region. The Galileo heatshield applied the same ablator configuration developed earlier for the Pioneer-Venus Probe. This consisted of chopped-molded carbon-phenolic in the nosecap region and tape-wrapped carbon-phenolic along the frustum. The carbon-phenolic material was modeled with a virgin density, $\rho_v = 1448$ kg/m^3 and a char density, $\rho_c = 1185$ kg/m^3 [3]. The lower thermal conductivity of the tape-wrapped carbon-phenolic would have ideally been used for the nosecap region as well; however, manufacturing limitations prevented its use [4]. Both the chopped-molded and tape-wrapped sections were fabricated using FM 5055G. The FM 5055 line of carbon-phenolic ablators was developed by the USAF in the late 1960s for use on Minutemen reentry vehicles [5]. To accommodate the radiative heating anticipated for Pioneer-Venus and Galileo, the FM 5055G material utilized a carbon opacified resin to prevent in-depth penetration of radiative heating [6, 7].

The chosen carbon phenolic thickness on the Galileo probe nose cone was 14.6 cm at the stagnation point, which decreased to 5.1 cm at the sphere-cone transition location. From there, the thickness increased to 5.4 cm at the shoulder. The recession history of the carbon phenolic heatshield was recorded with 10 analog resistance ablation detector (ARAD) sensors embedded in the forebody TPS. Additionally, four resistance thermometers were bonded to the inside of the structure to monitor the internal temperature [2, 3]. Locations of these sensors are shown in Fig. 1b. The ARAD data were successfully transmitted from the Galileo orbiter back to Earth after the planetary entry. Using the flight ARAD measurement data, Milos [2, 3] reconstructed the recession profile of the forebody heatshield.

During the design phase of the Galileo probe, state-of-the-art simulations for the time (early 1980s) provided the anticipated aerothermodynamic environments [1]. These simulations implemented the viscous shock layer equations for a thermochemical equilibrium gas with coupled radiation and ablation. A constant Schmidt number of 0.582 was applied.

The radiative heating was calculated using an equilibrium radiation code [8], which assumed tangent slab radiation transport. The shock-layer was considered fully turbulent and employed a two layer eddy-viscosity model, where the inner layer was based on Prandtl's mixing length concept and the outer law uses Clauser-Klebonoff expressions [1]. This model was introduced by Cebeci [9] and applies the inner layer model from the wall to where the inner and outer laws are equal, then applies the outer layer model for the remainder of the viscous layer. Steady-state equilibrium ablation was assumed, which applied a sublimation temperature curve-fit that was a function of both pressure and mass fraction of ablation species.

Figure 2 presents a comparison between the nominal simulated recession for design and the reconstructed recession [1–3]. The errors associated with the flight data are identified by Milos [2] as the sum of nominal measurement uncertainty plus the sensor bias uncertainty. This figure shows that the design prediction overestimates the stagnation region recession by 30%, while the frustum region was underestimated by as much as 50%. These discrepancies, especially the underestimation of the frustum recession, have motivated a number of post-flight studies.

Matsuyama et al. [10] performed a thermochemical equilibrium analysis that included coupled radiation and ablation. The radiative transport was computed with the tangent-slab approximation while the ablative product diffusion was modeled as binary with a constant Schmidt number of 0.582. Because of the massive ablation experienced by the Galileo probe, they implemented Park's injection induced turbulence model [11]. They showed that the addition of this model improved agreement with the measured frustum recession. This improved agreement was the result of a larger eddy viscosity from the augmented turbulence model enhancing the diffusion of ablation gases, which increases the boundary layer temperatures, therefore increasing C_2 and C_3 dissociation. The reduction in C_2 and C_3, which are strong absorbers, increases the radiative flux reaching the surface. Matsuyama et al. applied the He mole fraction measured by

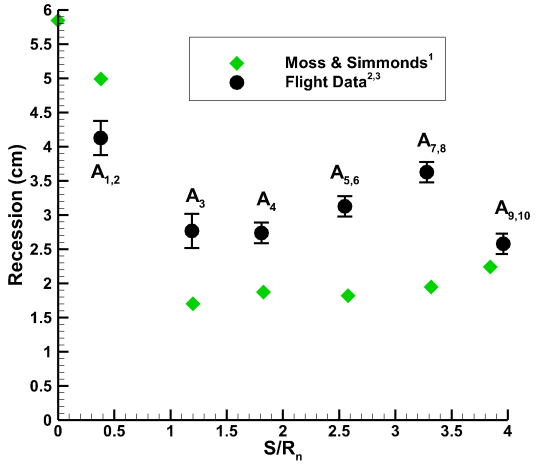

Fig. 2 Galileo probe forebody TPS recession [1–3].

the Galileo probe, which indicated a mole fraction of 13%, compared to the 11% assumed by Moss [1]. This higher He mole fraction also resulted in increased recession along the entire surface.

With the knowledge that C_3 can play a significant role in the radiative heating of the frustum region of the Galileo Probe, Matsuyama et al. [12] carried out an uncertainty analysis with regard to the absorption cross section for this particular species. In their study, they varied the absorption cross section of C_3 by 10 to 200% in both the VUV (Vacuum Ultraviolet) and Swings bands to study the effect on TPS recession at the peak heating trajectory point. They found that the uncertainty in the cross section data may impact the heating and recession by -11 to +25% at the stagnation point and -6 to +30% for the frustum region. Additionally, they found that the radiative heat flux prediction at the stagnation point was most sensitive to the Swings band while the frustum region responds almost identically to both the VUV and Swings bands.

Further investigation into the stagnation point recession history was conducted by Park [13], who analyzed the equilibrium composition, radiation absorption, and the effect of spallation for the Galileo trajectory. These analyses were performed using a viscous shock-layer code and a nose radius chosen to provide the appropriate shock standoff distance. Park employed the tangent-slab radiative transport approximation and computed the ablation product gas diffusion with the binary assumption and a constant Schmidt number of 0.582. He found that employing a modification to the original JANAF [14] coefficients, which corrects the values for two hydrogenous species, improved the prediction for stagnation point recession. An extension to the VUV absorption mechanisms for carbonaceous species also resulted in a small but noticeable improvement to the recession predictions. Additionally, when spallation was accounted for in the stagnation region, the recession predictions improved to values that nearly match the flight data.

Even with the significant advances made in these past studies, a number of potential modeling improvements remain. These include the removal of tangent slab assumptions, removal of the binary diffusion assumptions, and accounting for the effect of shape change. The impact of these improvements will be assessed in this work. To assess the impact of model-form uncertainties on the comparison with the Galileo recession measurements, numerous other modeling approaches will be investigated, including those related to diffusion, ablation, and radiation. Additionally, the impact of uncertainty in many model parameters on recession will be quantified and their individual impact assessed to guide future investments in uncertainty reduction. The results from this analysis will provide recommended practices for future investigations and analyses of this mission.

The next section outlines the analysis approach used in the current study. Section III presents an analysis of the results using the baseline model and provides comparisons of different modeling techniques and the significance of select physical phenomena. Section IV presents a parametric uncertainty analysis for the predicted recession. The last section provides important conclusions and identifies future work that may further improve predictions.

II. Simulation Parameters and Tools

This work applied the Langley Aerothermodynamic Upwind Relaxation Algorithm (LAURA) software, which is a finite-volume, Navier-Stokes flow solver [15]. This solver uses a second-order, upwind, discretization scheme with Roe's flux-difference splitting scheme and Yee's Symmetric Total Variation Diminishing (STVD) formulation of the inviscid flux. The flowfield was assumed to be steady state at each simulated trajectory point. The forebody boundary layer was modeled as fully-turbulent employing the Cebeci-Smith algebraic turbulence model [16]. Both of these assumptions are consistent with previous studies [1, 12, 13]. The wake flow was modeled as laminar as previous studies of backshell heating on planetary entry bodies with similar shape have shown that the primary heating source is radiation to the backshell surface, which is independent of the boundary layer state [17, 18]. The gas properties are modeled with a one temperature chemical nonequilibrium assumption. The Jovian atmosphere was modeled with 13.6% helium and 86.4% hydrogen, by volume.

The coupled ablation flowfield was modeled using the following 21 species: H_2, H, He, H^+, He^+, e^-, C, C_2, C_3, C_4, C_5, C^+, CH, C_2H, CH_2, C_2H_2, O, O_2, O^+, CO, and CO_2. The rate model used in this study is presented in the appendix in Table A1. The char rate is computed assuming chemical equilibrium between the carbon char and the gas at the wall [15, 19]. Steady-state ablation was assumed to compute the pyrolysis rate and heat conducted into the surface, as discussed further in section III. The elemental mass fractions assumed for the virgin carbon phenolic are 0.92, 0.06, and 0.02 for carbon, oxygen, and hydrogen, respectively. These are consistent with previous studies [1, 10, 12]. Steady-state equilibrium ablation was applied. Further details of the ablation model, including justification for the steady-state approximation, are provided in section III.A.1.

The radiation was modeled using the High-Temperature Aerothermodynamic Radiation (HARA) code [21, 22]. A ray-tracing approach [23] was applied for computing the radiative heating, while the tangent-slab approach was used to compute the divergence of the radiative flux, unless noted otherwise. The radiation mechanisms activated for the current study are presented in the appendix in Table A2. Coupled radiation was modeled in the flowfield energy equations. The uncertainties in this table are discussed later in section IV.

III. Assessment of Model-Form Uncertainties

This section presents details of the Galileo Probe simulations for the trajectory points listed in Table 2 [2]. The results are presented in a binary fashion where various radiation, ablation, and diffusion mechanisms are explored through activating or deactivating the particular mechanism and quantifying the comparative response from a baseline set of results. A set of best practices are presented based on the findings that can be utilized for further work on this problem.

For comparison of each of the modeling approaches, Table 3 identifies which approaches constitute the baseline model. These selected modeling approaches are relatively computationally efficient while providing an accurate

Table 2 Reconstructed Jovian atmosphere and trajectory data.

Time (s)	Altitude (km)	Velocity (m/s)	Density (kg/m^3)	Temperature (K)
40.35	190	46951.0	3.16e-5	165.0
43.79	170	46256.0	7.03e-5	165.8
47.36	150	44813.0	1.49e-4	168.9
49.21	140	43531.0	2.27e-4	164.3
51.16	130	41591.0	3.49e-4	160.8
53.23	120	38617.0	5.56e-4	153.6
55.52	110	34296.0	8.36e-4	156.6
58.19	100	28440.0	1.23e-3	160.6
61.57	90	21342.0	1.85e-3	160.1
66.35	80	13544.0	3.06e-3	147.8

comparison with the flight data. As will be shown, the approaches not selected for the baseline model do not contribute significantly to the final recession and come at significant computational cost for their negligible impact. Those approaches used in the baseline model are brought forward into the parametric uncertainty analysis in section IV. Figure 3 presents the baseline radiative and convective heating at various locations on the vehicle which will be referred to throughout this section. As indicated in Table 3, these solutions include coupled radiation and ablation. The following seven subsections (A-G) will discuss each of the modeling features in Table 3. The first two, both of which deal with ablation, are discussed together in the following subsection.

A. Impact of Coupled Ablation

To demonstrate the strong impact of coupled ablation for these cases, comparisons between simulations with and without coupled ablation are presented here for the stagnation line of the t = 53.2 s trajectory point. Figure 4 presents this comparison for the stagnation line temperatures. The surface blowing due to ablation is seen to increase the shock standoff distance for the ablating case. The decrease in the temperature gradient near the wall for the ablating case decreases the convective heating dramatically, as shown in a later figure. The boundary layer species for the ablating case are presented in Fig. 5 (note the change in scale of the horizontal axis to focus in on the boundary layer). The ablation products C_3, C_2H, and C provide partial blockage of the radiative heating. This blockage is shown in Fig. 6, which

Table 3 Activated modeling features for the assessment of model-form uncertainties.

	Coupled Ablation	Moving Boundary	Surface Ray Tracing	Multicomponent Diffusion	Ionization Potential Lowering	State-Specific H Modeling	Flowfield Ray Tracing	Precursor Absorption
Baseline Model	X	X	X	X	X			

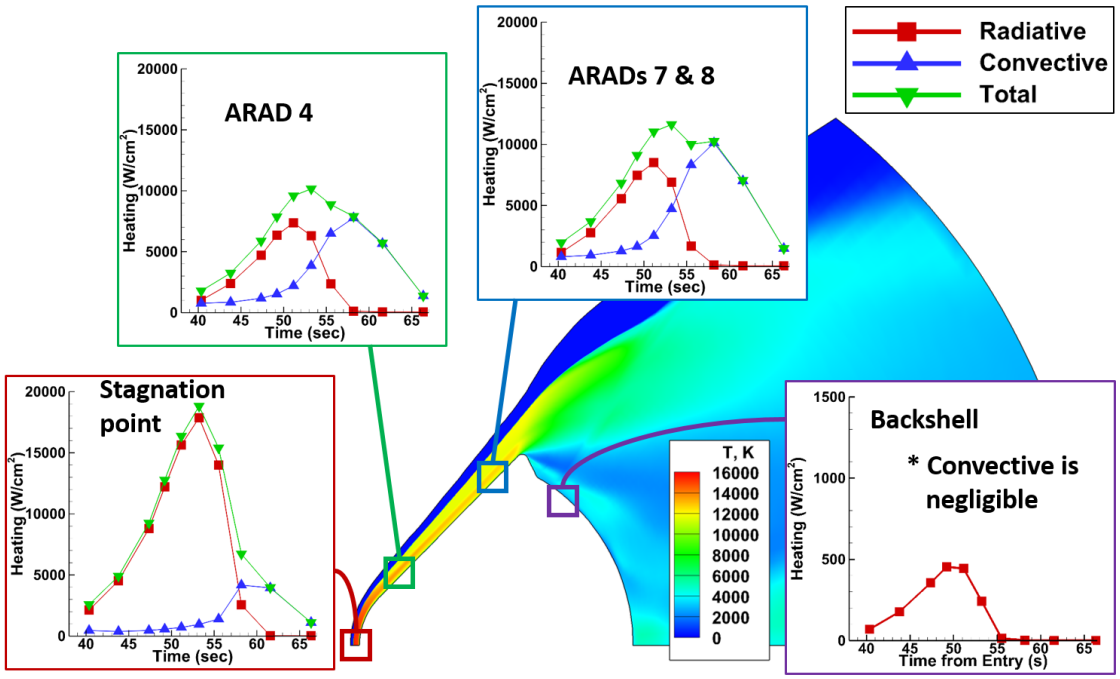

Fig. 3 Baseline heating values with coupled radiation and ablation.

compares the wall-directed radiative flux along the stagnation line for the ablating and nonablating cases. The strong absorption from ablation products is seen below 2 cm, where the ablating values decrease sharply below the nonablating values. The details of this ablation product absorption are shown in Fig. 7, which compares the wall-directed radiative flux spectrum at the wall. Spectral regions where the solid red line is below the solid black line indicate regions of ablation product absorption. In the 4 - 8 eV range, molecular band systems of C_3 and C_2H provide the absorption, while above 8 eV, it is provided by atomic photoionization from C. Figures 8 and 9 show the impact of ablation on the stagnation-point convective and radiative heating, respectively, through the trajectory. While the convective heating is reduced to negligible values throughout most of the trajectory due to ablation, the radiative heating is reduced by only 30%. However, as was shown in Fig. 3 the convective heating downstream of the stagnation-point is not negligible with coupled ablation. This is the result of lower ablation rates and the influence of turbulence downstream of the stagnation-point.

Although not shown in these figures, the afterbody location identified in Fig. 3 is found to be noticeably impacted by forebody ablation products. The radiative flux is roughly 25% greater for the ablating case, which is the result of increased radiative emission from ablation gases. The conclusion that ablation products impact the radiative heating on the backshell surface is consistent with previous work regarding super orbital entry velocity into Earth's atmosphere [18]. Note that a detailed analysis of the backshell heating is the subject of future work.

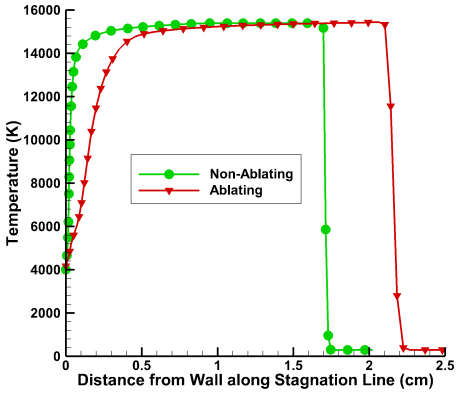

Fig. 4 Impact of ablation on stagnation line temperatures for the t = 53.2 s trajectory point.

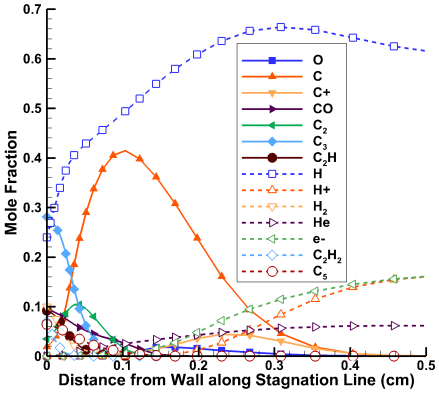

Fig. 5 Impact of ablation on stagnation line (zoomed in to the boundary layer) species mole fractions for the t = 53.2 s trajectory point.

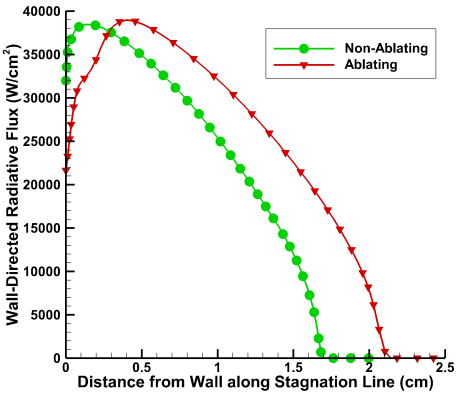

Fig. 6 Impact of ablation on stagnation line radiative flux for the t = 53.2 s trajectory point.

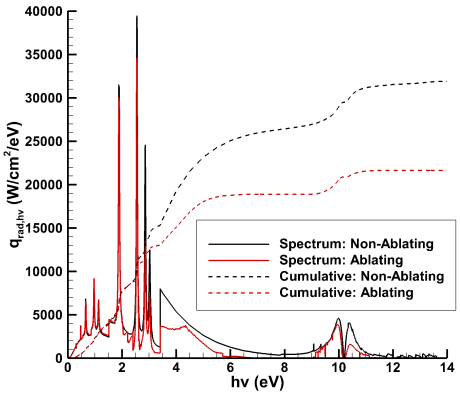

Fig. 7 Impact of ablation on stagnation point spectrum for the t = 53.2 s trajectory point.

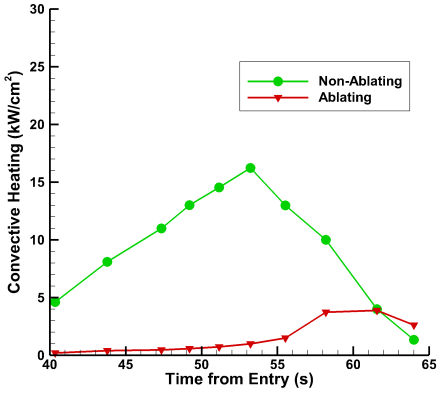

Fig. 8 Stagnation point convective heating with and without ablation.

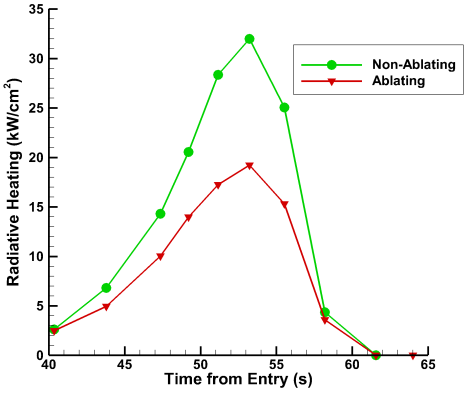

Fig. 9 Stagnation point radiative heating with and without ablation.

1. Evaluation of Ablation Quantities

The previous discussion focused on the impact of ablation on the radiative and convective heating. A significant aspect of these simulations is the evaluation of the ablation rates and wall temperatures, which are determined from the surface energy balance and equilibrium char constraint. The evaluation of these terms are discussed in this subsection. This discussion will emphasize the physical mechanisms that enable the ablator to accommodate the massive heating rates experienced by Galileo, which are not typically encountered by entry vehicles.

The surface energy balance for a charring ablator, which is illustrated in Fig. 10, is written as

$$q_c + \alpha q_{rad} - \epsilon\sigma {T_w}^4 - \dot{m}_c(h_w - h_c) - \dot{m}_g(h_w - h_g) - q_{cond} = 0 \tag{1}$$

The first two terms in this equation are the convective and absorbed radiative heating (α=0.9), which represents the applied heating that the ablator must accommodate. The third term is the reradiation from the ablator surface, which is a function of only the wall temperature and surface emissivity (ϵ = 0.9 for Galileo). The fourth and fifth terms are the enthalpy of injected char and pyrolysis gas minus their solid values, respectively. Finally, q_{cond} is the heat conducted into the ablator. For massively ablating cases such as Galileo, an often-applied approximation is the steady-state ablation approximation, which is the baseline approach in the current work. This assumption provides relationships for q_{cond} and $\dot{m}_g$, which would otherwise require an in-depth material response computation. The relationship for q_{cond} is:

$$q_{cond} = \dot{m}_c h_c + \dot{m}_g h_g \tag{2}$$

where h_g is the enthalpy of the pyrolysis gas before it mixes with the flowfield, and h_c is the enthalpy of the solid char,

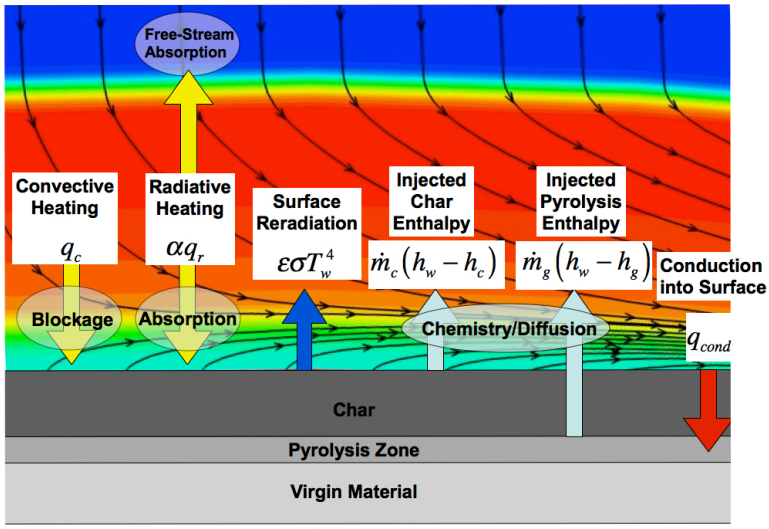

Fig. 10 Energy balance for a charring ablator.

with both terms evaluated at the wall temperature. The validity of this relationship is confirmed in Fig. 11, which applies LAURA's material response code for the stagnation line of the converged solutions (the $\dot{m}_c$ and T_w time histories were the inputs to the material response code, which then computed $\dot{m}_g$ and q_{cond}). The black line in this figure represents the error associated with this approximation. For this case, the peak error is less than 0.5 kW/cm^2, which is within 2.5% of the peak heating of 20 kW/cm^2. This confirms the validity of Eq. (2) for Galileo.

Applying Eq. (2) to Eq. (1), results in the following

$$q_c + \alpha q_{rad} - \epsilon \sigma {T_w}^4 - (\dot{m}_c + \dot{m}_g) h_w = 0 \tag{3}$$

This equation is solved in LAURA for the total ablation rate, $\dot{m} = \dot{m}_c + \dot{m}_g$. To solve this equation, T_w is evaluated based on the equilibrium char constraint, which also allows h_w to be computed. The elemental composition at the wall required for these equilibrium chemistry compositions is based on the flowfield diffusion, so the often applied assumption for Galileo that the elemental composition at the wall is equal to the ablation product elemental composition is removed. This is important for the flank regions on the forebody away from peak heating, where the ablation is weaker.

Once $\dot{m}$ is computed from Eq. (3), the $\dot{m}_c$ and $\dot{m}_g$ components are distinguished by applying the steady-state ablation relationship for $\dot{m}_g$:

$$\dot{m}_g = \left(1 - \frac{\rho_c}{\rho_v}\right) \dot{m} \tag{4}$$

where ρ_v and ρ_c are the virgin and char densities of the ablator, respectively. Applying the same material response simulation mentioned in the previous paragraph, Fig. 12 confirms that the char fraction, $\dot{m}_c/(\dot{m}_c + \dot{m}_g)$, is within ±10% of steady-state value defined by Eq. (4).

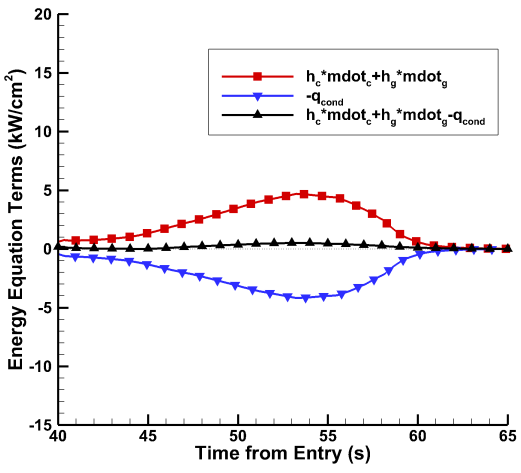

Fig. 11 Assessment of steady-state ablation approximation of Eq. (2) for surface energy balance terms.

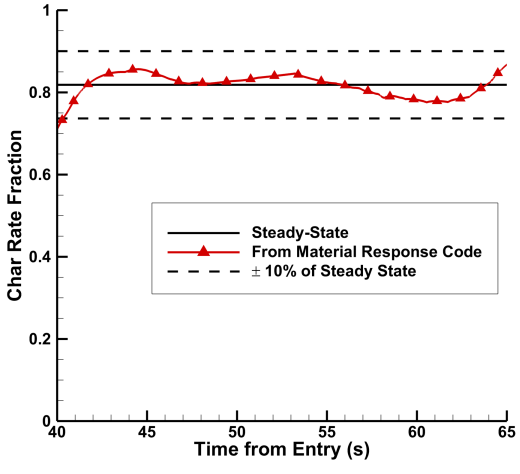

Fig. 12 Assessment of steady-state ablation approximation of Eq. (4) for $\dot{m}_g$.

To compare the contribution from each term in the steady-state energy balance of Eq. (3), Fig. 13 presents each term for the Galileo stagnation point through the trajectory. The positive convective and radiative heating drive the ablation processes represented by the negative terms. The most important ablation term is seen to be $\dot{m}_c h_w$. Figure 14 provides a breakdown of the contribution from individual species to this component, which shows that C_3 is the dominant species. Without $\dot{m}_c h_w$ (and $\dot{m}_g h_w$), the heat conducted into the surface, q_{cond}, would need to increase dramatically to satisfy Eq.(1), therefore allowing too much heat through the heatshield and destroying the vehicle (by increasing the bondline temperature of heatshield above an acceptable temperature limit).

2. Heatshield Shape Change Due to Ablation

Moss and Simmonds show that the large Galileo recession rates lead to a noticeable change in the heatshield geometry, with the large stagnation region rates producing a blunter nose [1]. Likewise, Milos [2] extrapolated the flight data to include stagnation point recession and found the nose to go from a 22.2 cm nose radius to 23.5 cm nose radius. This predicted blunter nose would impact the heating environment, where the stagnation point convective heating is proportional to the inverse of the nose radius and the radiative heating is directly proportional to the nose radius. Therefore, the radiative heating at the stagnation point increases with the blunter nose, while the convective heating decreases. To account for this behavior in the present baseline simulations, the surface recession was computed by integrating the mass injection prediction output from LAURA and dividing by the virgin density of the carbon phenolic TPS material given by

$$\Delta s_i^n = \frac{100}{\rho_v} \sum_{\tau=1}^{n} \left[\frac{1}{2} (\dot{m}_i^{\tau} + \dot{m}_i^{(\tau-1)}) \times (t^{\tau} - t^{(\tau-1)}) \right]$$

where the mass flow rate and trajectory time for τ_0 is defined to be $\dot{m}^0 = 0$ at $t^0 = 35.0$ seconds. Note that this approach is only valid for steady-state ablation, otherwise the char rate and density are applied instead.

Figure 15a shows a comparison of the final recession profiles computed with and without shape change while Fig. 15b shows the baseline and final recessed geometry with the nose radius labeled for each case. The coupled impact of shape change with surface heating distribution resulted in a sharpening of the nose. These results differ from that expected based on the original analysis from Moss and Simmonds and the extrapolated recession from Milos. The data show a slight increase in the recession near the $S/R_n = 0.1$ to 0.6 region compared to the stagnation point, which results in a slight sharpening of the nose. This sharper nose of the recessed geometry increases the convective heating at the stagnation point while decreasing the radiative heating. When comparing the final predicted recessed shape, there exists differences throughout the forebody. The higher predicted radiation on the nonrecessed nose results in even more predicted sharpening of the nose. The combined effect of the heat flux mechanisms on the different forebody shapes

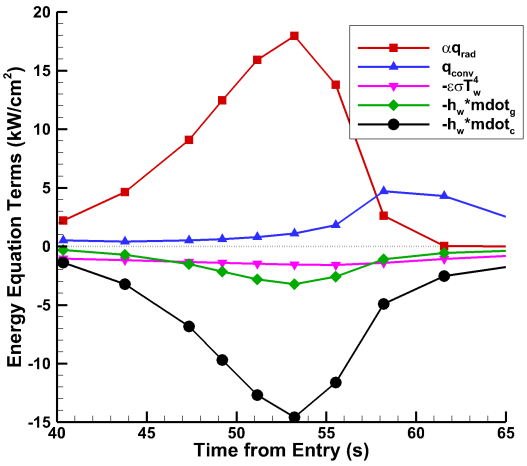

Fig. 13 The impact of ablation on stagnation point heating.

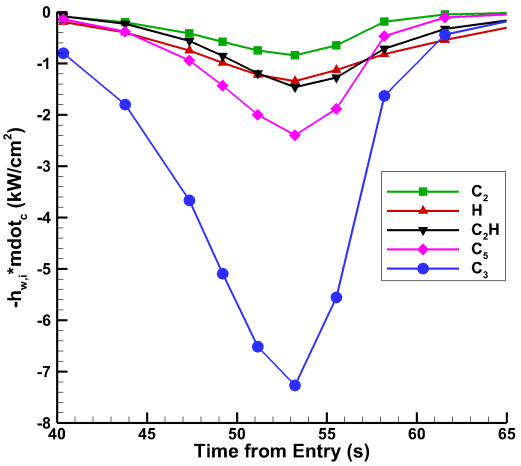

Fig. 14 Contributions of individual species to $\dot{m}_c h_w$.

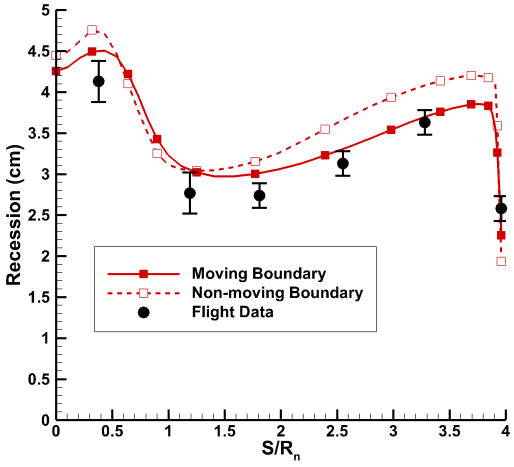

(a) Final recession profile

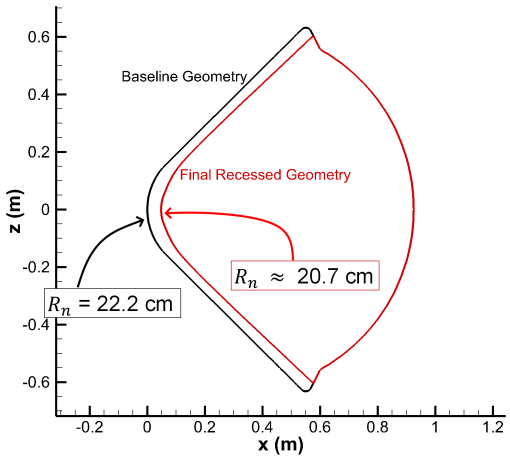

(b) Final Geometry Comparison

Fig. 15 Moving boundary results.

results in more overprediction at the stagnation line and the frustum region of the probe. The final recession magnitude, as predicted by the moving boundary analysis, more closely matches the flight data compiled by Milos [2].

B. Ray-Tracing vs. Tangent-Slab Approaches for Surface Radiative Heating

The tangent-slab approximation [24] is typically applied for computing the radiative flux and its divergence instead of the more rigorous ray-tracing approach [23] because it is over a factor of 100 more computationally efficient. Figure 16 compares the ray-tracing and tangent slab radiative heating values at selected surface locations. In the forebody, the

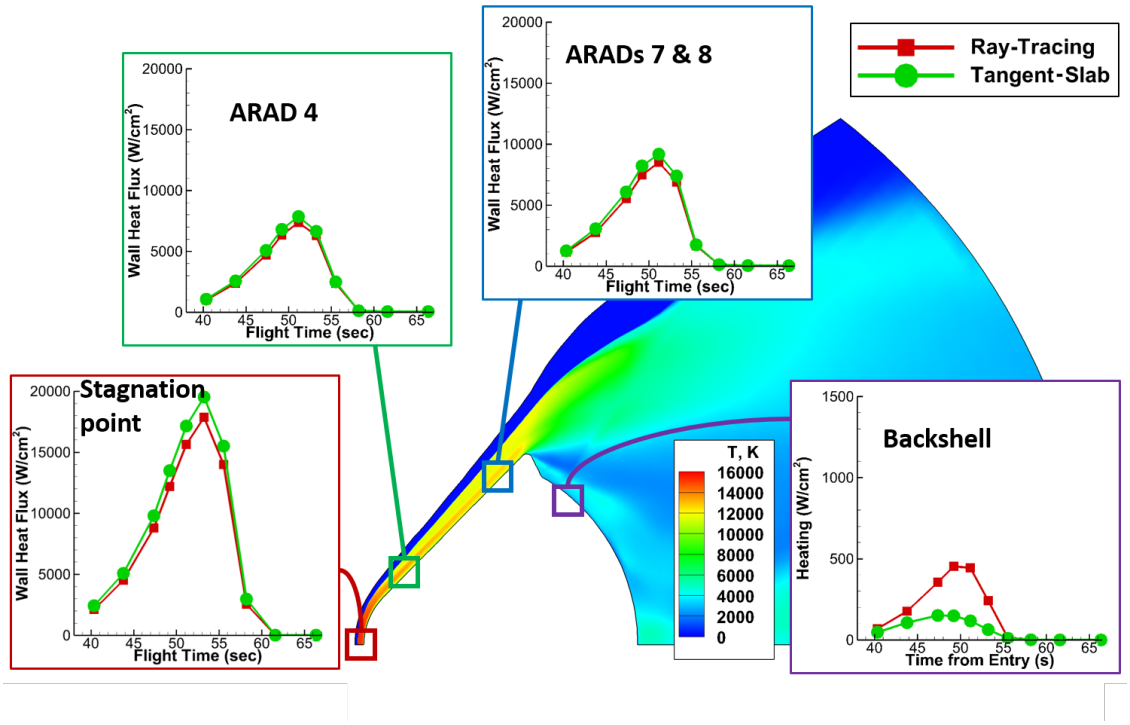

Fig. 16 Comparison of ray-tracing and tangent-slab radiative heating.

tangent-slab approach only slightly overpredicts the radiative heating. However, in the afterbody, the radiative heat flux is significantly underpredicted with tangent-slab by more than a factor of two at peak heating. This is in agreement with previous work by Johnston and Brandis [18], which showed that the tangent-slab approximation can result in significant errors in the afterbody region. To avoid the inaccuracies shown in this figure, ray-tracing was applied as the baseline approach. The impact of applying ray-tracing versus tangent slab on the final recession is shown in Fig. 17, where the lower heating from ray-tracing results in roughly 10% lower recession than tangent slab. This impact has not been included in past Galileo studies.

C. Flowfield Diffusion Modeling

Because of the mixing of boundary-layer edge and ablation product species, which have significantly different molecular weights, the importance of accurately modeling multicomponent diffusion could be significant for the massively ablating Galileo probe. All past analyses have assumed a constant Schmidt number of 0.582. The standard diffusion model in LAURA is the "approximate-corrected" approach to multicomponent diffusion [25]. This method has been found to provide a robust and computationally efficient approach for reproducing the results of the Stefan-Maxwell equations for Earth and Mars entry cases. However, the abundant presence of hydrogen in the Jovian atmosphere, which has a significantly lower molecular weight than the other species, makes the applicability of the "approximate-corrected" approach questionable. Therefore, the rigorous Stefan-Maxwell approach was applied in the present baseline model. As

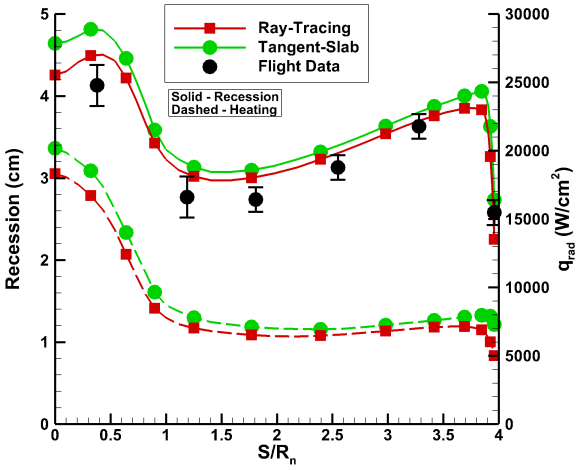

Fig. 17 Comparison of final recession profile and peak heating between ray-tracing and tangent-slab radiative heating.

an example of the impact of these diffusion models, Fig. 18 compares the convective heating resulting from both the "approximate-corrected" and Stefan-Maxwell approaches. Over a 50% increase is seen along the flank, which is the result of increased atomic hydrogen diffusion. The impact of this increased heating on the final recession is presented in Fig. 19, which shows a corresponding recession increase. This increased recession is larger along the flank than at the stagnation point, which provides a notable improvement in the profile shape relative to the flight data. This is the first Galileo study to remove the constant Schmidt number assumption.

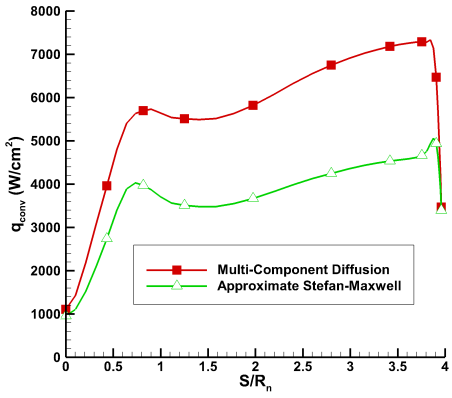

Fig. 18 Impact of diffusion models on convective heating at the peak heating point.

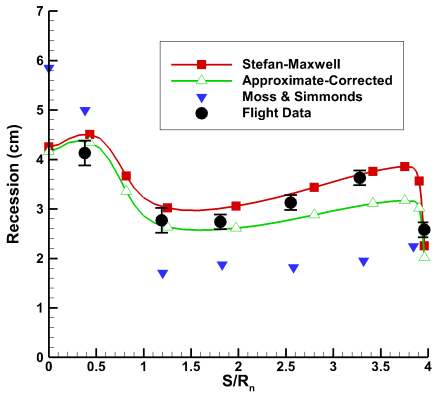

Fig. 19 Impact of diffusion models on final recession profile. [1–3].

D. Impact of Ionization Potential Lowering

The impact of ionization potential lowering at Galileo entry conditions is discussed by Nelson [26]. As the electron number density increases, the ionization potential for H decreases. This both reduces the number of electronic levels treated for evaluating the thermodynamic properties of H, but also reduces the heat of formation for H^+. Note that the thermodynamic properties of H and H^+ were recomputed using the NIST electronic levels to extend the temperature range to 50,000 K. The Unsöld approximation, which is discussed by Nelson [26], is applied here to model this ionization potential lowering. The primary impact of this lowering is an increase in the H^+ mole fraction and a decrease in shock layer temperatures, which combine to produce a decrease in the radiative heating. Figure 20a shows the impact of including ionization potential lowering on the recession and radiative heating. A 12% decrease in the peak stagnation point radiation results in a 10% decrease in the final recession. Figure 20b shows an appreciable growth in both radiation and the resultant recession at the stagnation region up to the peak heating trajectory point, after which the convective heating becomes dominant. Note that this phenomenon was accounted for in Park's study [13], which showed a similar trend at the stagnation-point.

E. State-Specific H Modeling

An assumption in the baseline simulation approach is that the electron-impact ionization rate for H is independent of the electron number density. Park [27] shows that this dependence is actually relatively strong for H, as well as its dependence on the escape factor. To capture these dependencies, a state-specific model for H was applied, following the approach of Johnston and Panesi [28] for N. This state-specific approach means that H is modeled with seven flowfield

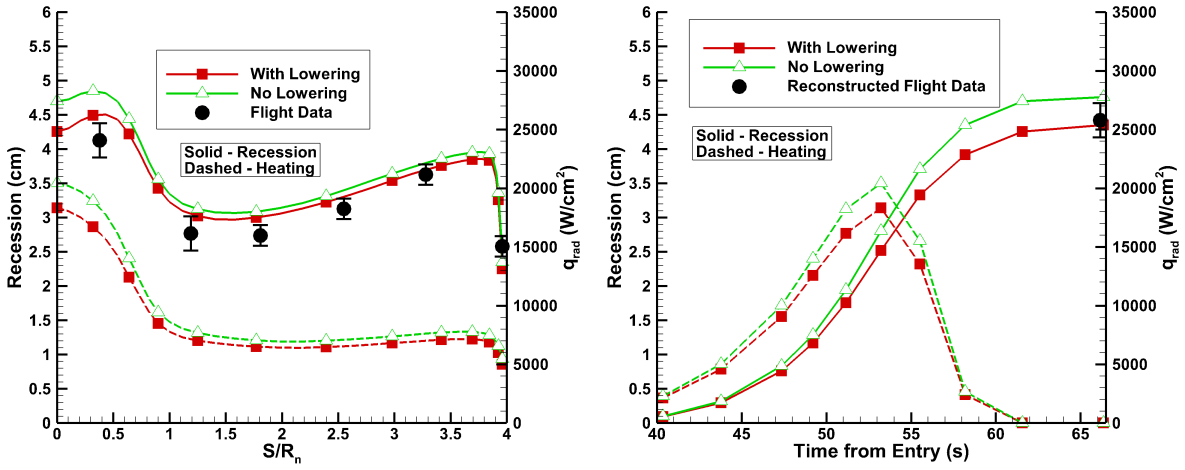

(a) Final Recession profile with peak radiative heat flux.

(b) Stagnation recession and radiative heat flux history.

Fig. 20 Impact of ionization potential lowering.

species, with each representing a group of closely spaced electronic states. These seven pseudo-species allow the electron number density and escape factor dependence to be captured, because each pseudo-species has its own electron impact ionization rate. Furthermore, radiative transitions between pseudo-species are captured. The present analysis applies the H model presented by Munafo et al. [29]. The result of applying the state-specific approach through the trajectory is compared in Fig. 21 with the conventional approach, which shows that the state-specific approach has a negligible impact on the final recession. This is a consequence of the shock layer being in strong thermochemical equilibrium. Although the conclusion that the flowfield is in strong equilibrium is apparent without applying the state-specific model, the present analysis confirms that the electron number density dependence of the electron-impact ionization rate for H, which is enabled by the state-specific model, does not enhance the nonequilibrium impact enough to negate this conclusion.

F. Coupled Flowfield Ray-Tracing

Previously in this section, the impact of computing the radiative heating on the surface of the probe using the ray-tracing [23] approach was described. The baseline approach to computing the divergence of the radiative flux when performing coupled radiation analyses with HARA is to use a tangent-slab approach [24]. While the emission at a point in the flowfield is only dependent on local conditions, the absorption depends on the incoming radiation from all directions. The tangent slab approach enforces the assumption that flowfield properties only vary along the direction normal to the surface. The ray-tracing approach accounts for the nonlocal variation of flow properties and the actual shape of the flowfield. While the tangent-slab assumption may seem significant, it is a necessary one as the computational cost of performing ray-tracing in the flowfield is orders of magnitude more expensive. Additionally, recent

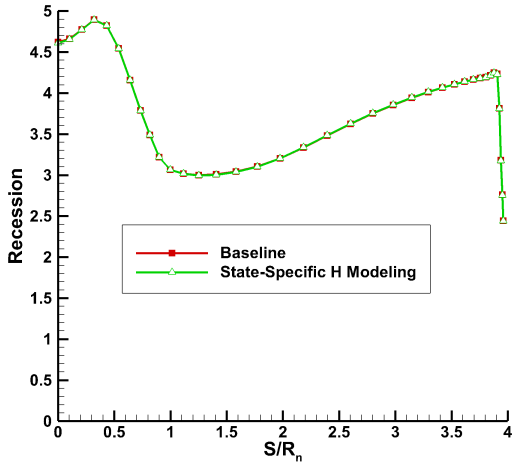

Fig. 21 Final recession profile from the state-specific H modeling uncertainty analysis.

work by Johnston and Mazaheri [30] showed the tangent-slab approach was able to accurately predict the divergence of the radiative flux in the flowfield for sample return entries into Earth.

Figure 22 shows the difference between computing the divergence of the radiative flux in the flowfield with ray-tracing and tangent-slab approaches. Note that, in both cases, the radiative heating at the wall is computed with ray-tracing. This figure shows indistinguishable differences between the two approaches. As a result, the baseline model does not include computing the divergence of the radiative flux with the ray-tracing approach, as the tangent-slab approach is sufficiently accurate while being significantly less computationally expensive.

G. Impact of Freestream Radiative Absorption

To assess the impact of radiative absorption in the freestream, also referred to as the precursor absorption, the 51.16 s case is considered with the flowfield grid extended one body radius in front of the stagnation point. Furthermore, the photochemical source terms are computed by HARA and applied to the flowfield, in addition to the divergence of the radiative flux, as discussed by Johnston et al. [31]. The primary photochemical processes in the precursor for Jupiter entry are the photodissociation of H_2 and the photoionization of H. To compute the photodissociation for H_2, the cross sections presented by Heays et al. [32] are applied. These values result in significant absorption above 11.8 eV (or below 105 nm). The standard HARA model for the photoionization cross sections for H are applied. To allow the thermochemical nonequilibrium behavior characteristic of the radiative precursor, the present case applies the two temperature model, instead of the one temperature model applied throughout this work.

Figure 23a presents the vibrational-electronic temperatures in the precursor, while Fig. 23b presents both temperatures along the stagnation-line. These figures show that a peak vibrational-electronic temperature of 2500 K is reached

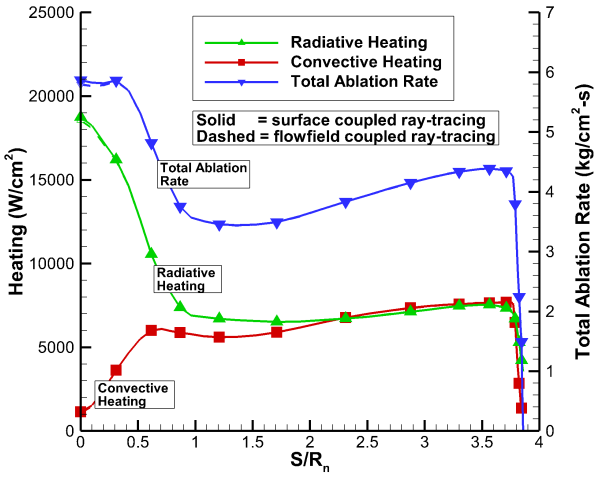

Fig. 22 Impact of coupled flowfield ray-tracing at 53.23 s.

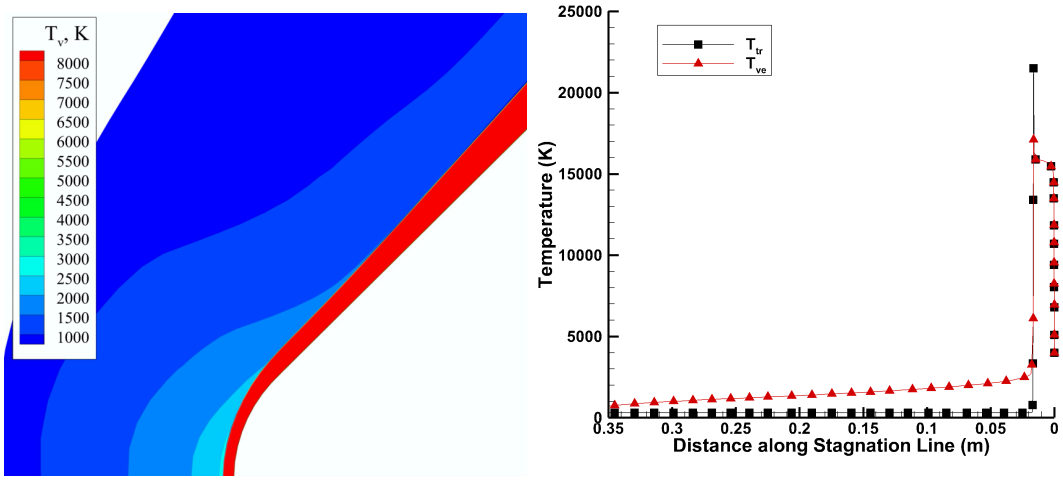

(a) Flowfield vibrational-electronic temperature.

(b) Stagnation line temperatures.

Fig. 23 Impact of precursor absorption on the vibrational-electronic temperature for the 51.16 s case.

in the precursor. Note that no equilibration is seen between the two temperatures in the precursor, so that the translation-rotational temperature remains at the free-stream value. The photodissociation results in less than 1% dissociation of H_2 in the precursor, while precursor photoionization leads to a electron mass fraction of 1×10^{-6} prior to the shock. These higher temperatures and minor photochemistry differences result in a negligible change in the shock layer temperatures and resulting radiation. An increase in less than 1% in the stagnation point radiative heating is predicted for the precursor case relative to the no-precursor case. This justifies neglecting the precursor throughout the remainder of this study.

IV. Parametric Uncertainty Analysis

This section describes the parametric uncertainty analysis used to assess the impact of uncertainties in physical quantities, such as kinetic rates, line strengths of atomic species, oscillator strengths of molecular species, heats of formation, and turbulent Schmidt number. Each of these uncertainty sources is described and their combined impact on the final recession prediction is discussed. Note that each of the uncertainty sources identified in this study was assumed epistemic, as there is not sufficient data to justify a classical statistical analysis. Additionally, the heating is assumed to have a monotonic dependency on each of the uncertain parameters, which is physically valid for the uncertainty sources considered here.

A. Flowfield Chemical Reaction Rate Uncertainties

The rate model used in this work is shown in the appendix in Table A1. These rates and their associated uncertainties are compiled from multiple sources [33–35]. All previous studies of the Galileo probe aerothermal environment have

assumed the flowfield to be in thermochemical equilibrium [1, 12, 13]. Furudate et al. [36] investigated the impact of chemical nonequilibrium for Galileo conditions without ablation, but concluded the effects have little impact on surface radiative heating. In the current work, a nonequilibrium model has been employed for completeness, and thus removes any uncertainties associated with assuming equilibrium throughout the trajectory.

Due to the relative importance of the electron and H^+ number densities, a more detailed investigation of the H ionization rate was warranted. Figure 24 shows a comparison of different rates found in the literature [27, 35, 37, 38]. The baseline rate used in the current study was the one proposed by Park et al. [35] in 2001, which was deduced from experimental data. The rate by Nelson [38] was computed for a neutral reaction process. The Leibowitz [37] rate is often used for analyzing H_2-He freestream flows, but is much lower than the rate by Park; however, Park [39] discusses that there may have been issues with the experiment by Leibowitz due to the shock-tube driver gas strongly radiating. This may introduce larger errors for high shock velocity scenarios. The detailed rate model by Park [27] from 2004 includes the impact of electron number density and Lyman line absorption and, therefore, has a wider applicability than a single rate.

The effect of lowering the H ionization rate by one order of magnitude is illustrated in Fig. 25, which shows the temperature and wall-directed radiative flux along the stagnation line and a line normal to the flank. Notice that, at the 53.23 s trajectory point, the shock-layer temperature and wall directed radiative flux is mostly unaffected by the change in ionization rate. Along the stagnation line, there is slightly higher radiative flux, post-shock, but this difference is negated at the wall due to absorption in the ablation layer. This result indicates that the flowfield is essentially in chemical equilibrium and, thus, is not sensitive to lowering or raising the ionization rate. The same argument can be

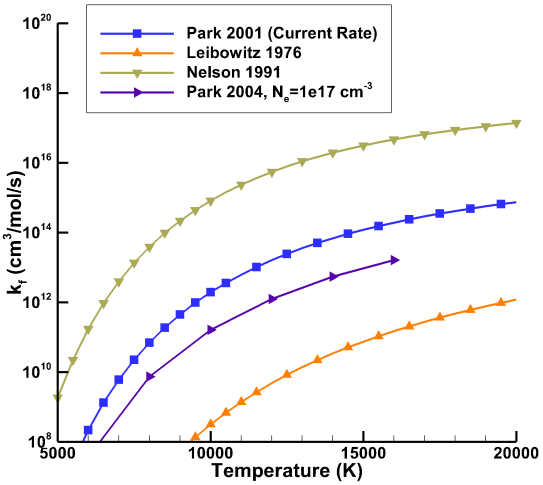

Fig. 24 H ionization rates by electron impact.

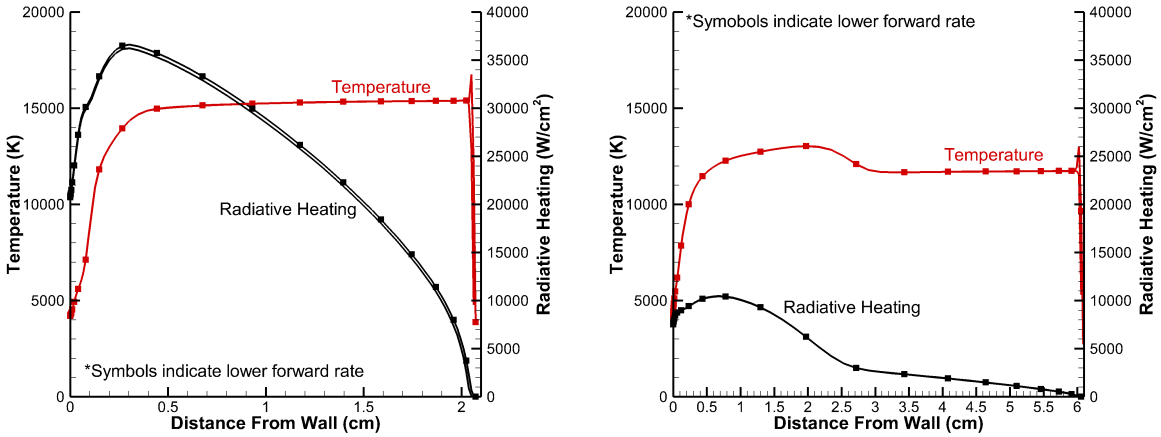

(a) Stagnation line.

(b) Line normal to flank.

Fig. 25 Impact of lowering the H ionization rate by 1 order-of-magnitude at 53.23 s.

made for other rates and species in both the freestream gas region of the shock and ablation layer. As a result, while each mechanism in the rate model has uncertainty, this uncertainty has a negligible impact on the forebody recession.

B. Atomic Lines and Photoionization Uncertainties

Atomic line and photoionization uncertainties for H and C are listed in Table A2. Detailed line data and estimated uncertainties for each line are given by Wiese et al. for C [40] and by Wiese and Fuhr [41] for H. A review of theoretical atomic carbon photoionization cross sections was made by Escalante [42]. These, along with experimental measurements of carbon by Marrone and Wurster [43] and of Hydrogen by Palenius et al. [44] indicated a ±20% uncertainty in both cross-sections was appropriate.

Figure 26 shows the parametric impact of uncertainty associated with atomic line strength and a photoionization cross section. Notice that the impact of the H photoionization cross section uncertainty has the greatest impact on the radiative heating. This is expected as a primary source of emission from the flowfield is from the H continuum. H line strengths have relatively low impact due to their low uncertainty magnitude. The impact of C, while insignificant at the stagnation point, does have some importance on the heatshield flank.

C. Molecular Band Uncertainties

The molecular band systems applied in this study are listed Table A2, along with their associated uncertainties. These uncertainties are found from other sources, in particular, from work by Johnston et al. for Mars Entry [45] and Earth entry [46]. The latter provides a detailed discussion of the magnitude of the uncertainties.

For the uncertainty in C_3, recent additional information [47] has become available and, therefore, the associated

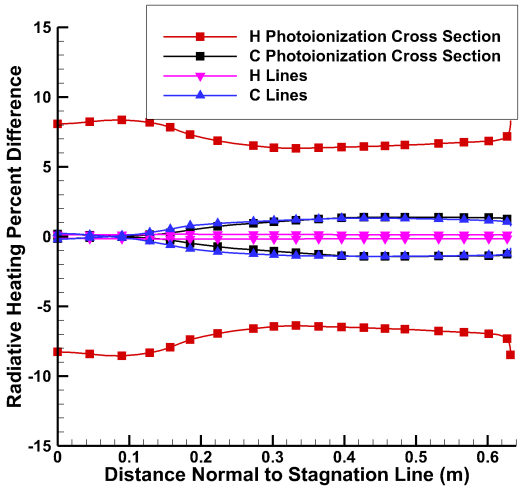

Fig. 26 Parametric radiation uncertainty of key atomic line systems at 53.23 s.

uncertainty warranted reevaluation. Shinn [48] measured the absorption cross-section of C_3 in the UV range, which showed to be about an order of magnitude higher than predicted by Arnold et al. [49]. Recent ab initio calculations by Kulakhmetov [47] resulted in an absorption cross-section about an order of magnitude less than the data collected by Shinn. Therefore, the uncertainty in the C_3 UV band was chosen to be one order of magnitude less than the Shinn data; however, with no additional upper uncertainty as was used in previous work [46].

A similar argument was made for the C_3 Swings system. Previous experimental measurements [50–52] were performed at temperatures below 4000 K and all resulted in peak absorption cross section magnitudes varying within 50% of each other. Shinn [48] also collected one data point in the Swings wavelength range. The ab initio calculations by Kulakhmetov [47] also resulted in lower than measured absorption cross section. Using all of this information, an uncertainty in the absorption cross section of plus 100% and minus one order of magnitude was applied to the C_3 swings system.

The resulting parametric impact of molecular band system uncertainties on radiative heating is shown in Fig. 27 at the 53.23 s trajectory point. In total, only the C_2H and C_3 band system uncertainties have significant impact on the overall radiative heating. All others have a less than 1% impact. Based on the discussion in section III.A.1 and the magnitudes of the uncertainties in these band systems, this result is expected. C_2H and C_3 are significant absorbers of incoming flowfield radiation. Other species, such as CO, have relatively low associated uncertainty and do not significantly impact the radiative heating and subsequent ablation. The resulting impact of all the molecular band uncertainties will be shown at the end of this section with all of the uncertainties rolled-up to provided a final estimate of the predicted recession uncertainty.

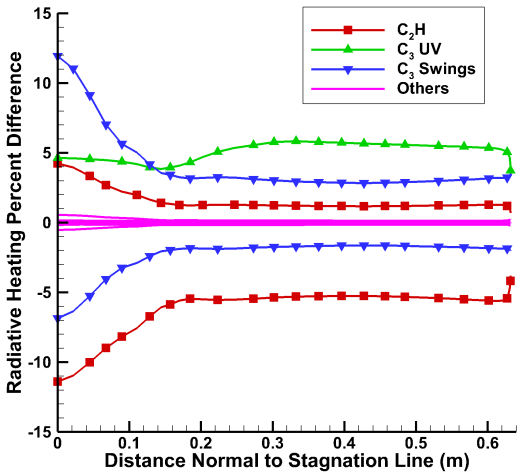

Fig. 27 Parametric radiation uncertainty of key molecular band systems at 53.23 s.

D. Heats of Formation for C_2, C_3, and C_2H

The heat of formation of three ablation products, namely C_2, C_3, and C_2H, have been shown to possess significant uncertainty [53–55]. This uncertainty may impact the species compositions within the ablation layer, which in turn impacts the radiative heat flux on the surface, as shown by Moss and Simmonds [1]. The uncertainties used in this study, which were given by Gurvich et al. [53], are listed in Table 4. These are also in agreement with uncertainties identified more recently by Sharma et al. [55]. Johnston et al. [46] used these same uncertainties for a Mars return Earth entry scenario but did not find significant impact due to relatively low ablation rates. The impact of the heat of formation uncertainties on the Galileo probe predictions is shown in Fig. 28 for the peak heating point at 53.23 s.

The total uncertainty due to heats of formation is about ± 0.05 kg/m^2-s, which amounts to less than ± 1% mass loss per unit area at the stagnation point. Moss and Simmonds [1] showed that the heat of formation uncertainty had a significant impact with more than 5% difference in stagnation point radiative flux; however, their uncertainty was on the order of 20% compared to the current uncertainty magnitudes of just over 1%.

E. Turbulent Schmidt Number Uncertainty

The exact value of the turbulent Schmidt number (Sc_T), especially for high enthalpy flows, is a subject of debate. Edquist et al. [56] found that published values of the turbulent Schmidt number typically fall in the range of $0.5 <= Sc_T <= 1.0$. The current baseline solution employs a value of $Sc_T = 0.9$. Sensitivity in the predicted heating is due to the value of the turbulent Schmidt number influencing the intensity of boundary layer mixing while increasing diffusion rates of species to the wall. The impact of the turbulent Schmidt number uncertainty is shown in Fig. 29. The upper uncertainty bound for the turbulent Schmidt number in this study was $Sc_T = 1.0$, which lowers the total recession

Table 4 Uncertain thermodynamic properties.

Species	$\Delta_f H(0)$, (kJ/mol)	Uncertainty
C_2	822.4	+/-1.22%
C_3	831.0	+/-1.56%
C_2H	565.0	+/-1.10%

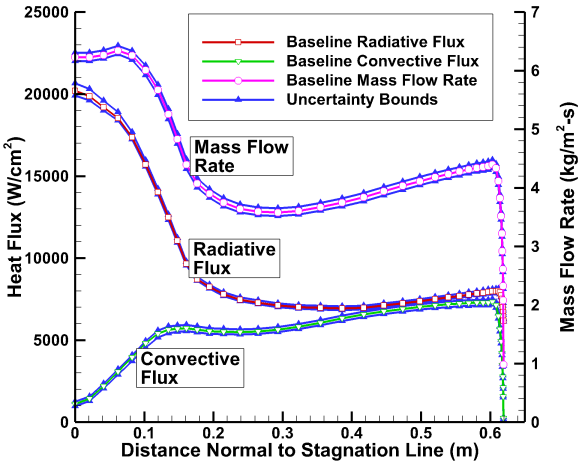

Fig. 28 Impact of carbonaceous molecule heat formation uncertainty at 53.23 s.

of the surface. The lower uncertainty bound was $Sc_T = 0.8$, which increases the recession of the surface. Note that the full range of uncertainty identified by Edquist et al. [56] was not considered here. Because lowering the turbulent Schmidt number has the effect of increasing the recession, lowering the lower values below the current nominal of 0.9 moves the predicted total recession further from the flight data. Therefore, limiting the lower uncertainty bound to 0.8 was deemed appropriate.

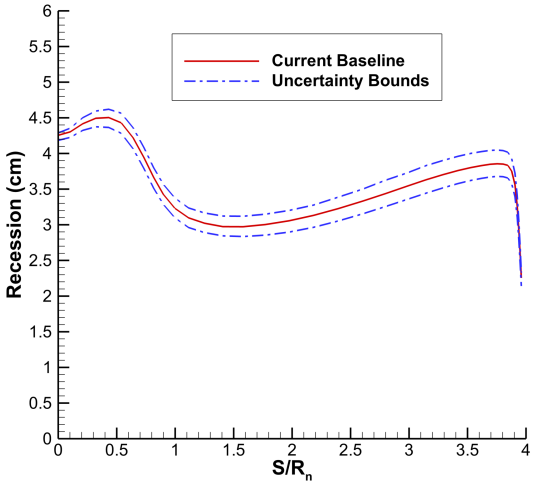

Fig. 29 Turbulent Schmidt number uncertainty results.

F. Total Parametric Uncertainty

The combined impact of the uncertainty sources described in this section are shown in Fig. 30 compared to the flight data and the pre-flight predictions by Moss and Simmonds [1]. Note that this uncertainty value also includes the uncertainty associated with assuming a ± 10% char rate uncertainty as suggested in section III.A.1. At the stagnation point, the uncertainty is dominated by radiation sources. From the discussions above, the dominant radiation uncertainty sources are the photoionization cross section of H and oscillator strengths of the C_3 systems. On the flank, the radiation accounts for about 30% of the uncertainty, while the heat of formation and char rate uncertainties account for 15% and 5%, respectively. The effect from the turbulent Schmidt number uncertainty accounts for 50% of the overall uncertainty bounds on the flank where the intensity of the boundary layer mixing and diffusion rate are affected. The inclusion of these uncertainties, along with the improved baseline modeling approach described in section III provides a remarkable prediction of TPS recession when compared to the flight data, which has yet to be achieved by previous studies.

V. Conclusions

The current analysis provides the most accurate recession prediction for the Galileo Probe TPS material to date. Convective heating was shown to be a significant contributor to total surface heating away from the stagnation-point, particularly later in the trajectory. Inclusion of modeling approaches not previously considered, such as a moving wall boundary due to ablation, multi-component diffusion modeling, and ray-tracing, significantly improve baseline model accuracy when compared to the flight recession data. The uncertainty analysis provided in this study highlights the impact of variability in many physical modeling parameters, including those related to the flowfield rate model, radiation modeling, and heats of formation of carbon-based species. Overall, the modeling approaches discussed in this paper

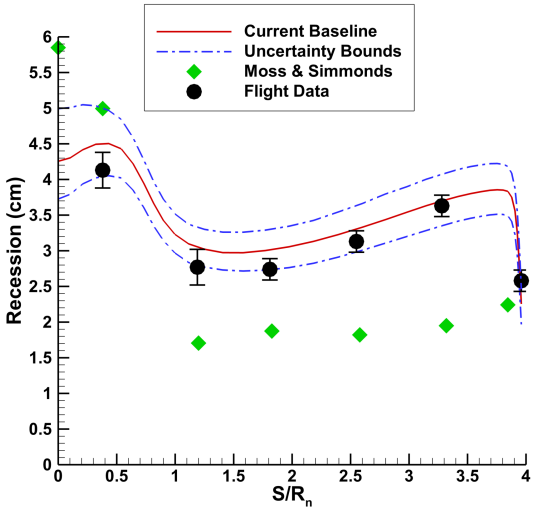

Fig. 30 Predicted recession with uncertainty compared to flight data.

outline an accurate approach to predicting TPS recession during similar entry conditions. Further model improvements, such as TPS spallation modeling, injection induced turbulence modeling, and inclusion of heavier carbon-based species, are the subject of future work; however, these are expected to have minimal impact given the results of this study.

References

[1] Moss, J. N., and Simmonds, A. L., "Galileo Probe Forebody Flowfield Predictions," AIAA paper 82-0874, 1982.

[2] Milos, F. S., "Galileo Probe Heat Shield Ablation Experiment," *Journal of Spacecraft and Rockets*, Vol. 34, No. 6, 1997, pp. 705–713. doi:10.2514/2.3293.

[3] Milos, F. S., Chen, Y. K., Squire, T. H., and Brewer, R. A., "Analysis of Galileo Probe Heatshield Ablation and Temperature Data," *Journal of Spacecraft and Rockets*, Vol. 36, No. 3, 1999, pp. 298–306. doi:10.2514/2.3465.

[4] Brewer, R. A., "Selection of a Heat Protection System for Venusian Entry," AIAA Paper 1975-731, 1975.

[5] Venkatapathy, E., and Laub, B., "Thermal Protection System: Carbon Phenolic," Presentation to the OPAG Community, 2009.

[6] Brewer, R. A., and Brant, D. N., "Thermal Protection System for the Galileo Mission Atmospheric Entry Probe," AIAA Paper 1980-0358, 1980.

[7] Legendre, P. J., Holtz, T., and Sikra, J. C., "Heatshield Material Selection for Advanced Ballistic Reentry Vehicles," AIAA/ASTM 11th Space Simulation Conference, NASA Johnson Space Center, Houston, TX., 1980.

[8] Nicolet, W. E., "Advanced Methods for Calculating Radiation Transport in Ablation-Product Contaminated Boundary Layers," NASA CR 1656, 1970.

[9] Cebeci, T., "Behavior of Turbulent Flow Near a Porous Wall With Pressure Gradient," *AIAA Journal*, Vol. 8, No. 12, 1970, pp. 2152–2156. doi:10.2514/3.6079.

[10] Matsuyama, S., Ohnishi, N., Sasoh, A., and Sawada, K., "Numerical Simulation of Galileo Probe Entry Flowfield with Radiation and Ablation," *Journal of Thermophysics and Heat Transfer*, Vol. 19, No. 1, 2005, pp. 28–35. doi:10.2514/1.10264.

[11] Park, C., "Injection-Induced Turbulence in Stagnation Point Boundary Layers," *AIAA Journal*, Vol. 22, No. 2, 1984, pp. 219–225. doi:10.2514/3.8371.

[12] Matsuyama, S., Furudate, M., and Fujita, K., "Numerical Attempt for Reproducing the Surface Recession Data of Galileo Probe," AIAA Paper 2007-0414, 2007.

[13] Park, C., "Stagnation-Region Heating Environment of the Galileo Probe," *Journal of Thermophysics and Heat Transfer*, Vol. 23, No. 3, 2009, pp. 417–424. doi:10.2514/1.38712.

[14] Perini, L. L., "Curve Fits of JANAF Thermochemical Data," Tech. rep., Applied Physics Lab Rept. ANSP M-5, Sep. 1972.

[15] Mazaheri, A., Gnoffo, P. A., Johnston, C. O., and Kleb, B., "Laura Users Manual: 5.5-76679," Tech. rep., NASA TM 217800, May 2017.

[16] Cebeci, T., and Smith, A. M. O., "A Finite-Difference Solution of the Incompressible Turbulent Boundary-Layer Equations by an Eddy-Viscosity Concept," *Computation of Turbulent Boundary Layers*, AFOSR-IFP-Stanford Conference, 1968, pp. 346–355.

[17] West IV, T. K., Johnston, C. O., and Hosder, S., "Uncertainty and Sensitivity Analysis of Afterbody Radiative Heating Predictions for Earth Entry," *Journal of Thermophysics and Heat Transfer*, Vol. 31, No. 2, 2017, pp. 294–306.

[18] Johnston, C. O., and Brandis, A. M., "Feature of Afterbody Radiative Heating for Earth Entry," *Journal of Spacecraft and Rockets*, Vol. 52, No. 1, 2015, pp. 105–119.

[19] Johnston, C. O., Gnoffo, P. A., and Mazaheri, A., "A Study of Ablation-Flow Field Coupling Relevant to the Orion Heatshield," AIAA paper 2009-4318, 2009.

[20] S., M., Y., S., N., O., A., S., and K., S., "Multiband Radiation Model for Simulation of Galileo Probe Entry Flowfield," *Journal of Thermophysics and Heat Transfer*, Vol. 20, No. 3, 2005, pp. 611–614. doi:10.2514/1.16432.

[21] Johnson, C. O., Hollis, B. R., and Sutton, K., "Spectrum Modeling for Air Shock-layer Radiation at Lunar-Return Conditions," *Journal of Spacecraft and Rockets*, Vol. 45, No. 5, 2008, pp. 865–878.

[22] Johnson, C. O., Hollis, B. R., and Sutton, K., "Non-Boltzman Modeling for Air Shock Layers at Lunar Return Conditions," *Journal of Spacecraft and Rockets*, Vol. 45, No. 5, 2008, pp. 879–890.

[23] Mazaheri, A., Johnston, C. O., and Sefidbakht, S., "Three-Dimensional Radiation Ray-Tracing for Shock-Layer Radiative Heating Simulations," *Journal of Spacecraft and Rockets*, Vol. 50, No. 3, 2013, pp. 485–493.

[24] Johnston, C. O., "Improved Exponential Integral Approximation for Tangent-Slab Radiation Transport," *Journal of Thermophysics and Heat Transfer*, Vol. 24, No. 3, 2010, pp. 659–661.

[25] Sutton, K. C., and Gnoffo, P. A., "Multi-Component Diffusion with Application To Computational Aerothermodynamics," AIAA paper 98-2575, 1998.

[26] Nelson, H. F., "Effects of Reduction of the Ionization Potential on Solution of the Rankine-Hugoniot Equations for Jovian Entry," *Journal of Quantitative Spectroscopy and Radiative Transfer*, Vol. 16, No. 12, 1976, pp. 1061–1064.

[27] Park, C., "Effects of Lyman Radiation on Nonequilibrium Ionization of Atomic Hydrogen," AIAA Paper 2004–2277, 2004.

[28] Johnston, C. O., and Panesi, M., "Impact of State-Specific Flowfield Modeling on Atomic Nitrogen Radiation," *Physical Review Fluids*, Vol. 1, No. 013402, 2018.

[29] Munafo, A., Mansour, N., and Panesi, M., "A Reduced-order NLTE Kinetic Model for Radiating Plasmas of Outer Envelopes of Stellar Atmsopheres," *The Astrophysical Journal*, Vol. 838, No. 126, 2017.

[30] Johnston, C. O., and Mazaheri, A., "Impact of Non-Tangent-Slab Radiative Transport on Flowfield–Radiation Coupling," *Journal of Spacecraft and Rockets*, Vol. 55, No. 4, 2018, pp. 899–913. doi:10.2514/1.A34072.

[31] Johnston, C. O., Gnoffo, P. A., and Mazaheri, A., "Influence of Coupled Radiation and Ablation on the Aerothermodynamic Environment of Planetary Entry Vehicles," VKI Lecture STO-AVT-218, 2013.

[32] Heays, A. N., Bosman, A. D., and van Dishoek, E. F., "Photodissociation and Photoionization of Atoms and Molecules of Astrophysical Interest," *Astronomy and Astrophysics*, Vol. 602, No. A105, 2017.

[33] Fujita, K., Yamada, T., and Ishii, N., "Impacts of Ablation Gas Kinetics on Hyperbolic Entry Radiative Heating," AIAA Paper 2006–1185, 2006.

[34] Gokcen, T., "N_2-CH_4-Ar Chemical Kinetic Model for Simulations of Atmospheric Entry to Titan," AIAA Paper 2004–2469, 2004.

[35] Park, C., Jaffe, R. L., and Partridge, H., "Chemical-Kinetic Parameters of Hyperbolic Earth Entry," *Journal of Thermophysics and Heat Transfer*, Vol. 15, No. 1, 2001, pp. 76–90.

[36] Furudate, M., Jeung, I. S., and Matsuyama, S., "Nonequilibrium Calculation of Flowfield over Galileo Probe," AIAA Paper 2006-0383, 2006.

[37] Leibowitz, L. P., and Kuo, T., "Ionizational Nonequilibrium Heating During Outer Planetary Entries," *AIAA Journal*, Vol. 14, No. 9, 1976, pp. 1324–1329.

[38] Nelson, H. F., Park, C., and Whiting, E. E., "Titan Atmospheric Composition by Hypervelocity Shock-Layer Analysis," *Journal of Thermophysics and Heat Transfer*, Vol. 5, No. 2, 1991, pp. 157–165.

[39] Park, C., "Nonequilibrium Ionization and Radiation in Hydrogen-Helium Mixtures," AIAA Paper 2010–0814, 2010.

[40] Wiese, W. L., Fuhr, J. R., and Deters, T. M., "Atomic Transition Probabilities of Carbon, Nitrogen, and Oxygen," *Journal of Physical and Chemical Reference Data*, , No. 7, 1996.

[41] Wiese, W. L., and Fuhr, J. R., "Accurate Atomic Transition Probabilities for Hydrogen, Helium, and Lithium," *Journal of Physical and Chemical Reference Data*, Vol. 38, No. 3, 2009, pp. 565–720. doi:10.1063/1.3077727.

[42] Escalante, V., "Photoionization of Excited States of Neutral Atomic Carbon and Singly Ionized Nitrogen," *Atomic Data and Nuclear Data Tables*, Vol. 51, No. 1, 1992, pp. 1–57.

[43] Marrone, P. V., and Wurster, W. H., "Measurement of Atomic Nitrogen and Carbon Photoionization Cross Sections Using Shock Tube Vacuum Ultraviolet Spectroscopy," *Journal of Quantitative Spectroscopy and Radiative Transfer*, Vol. 11, 1971, pp. 327–348.

[44] Palenius, H. P., Kohl, J. L., and Parkinson, W. H., "Absolute measurement of the photoionization cross section of atomic hydrogen with a shock tube for the extreme ultraviolet," *Phys. Rev. A*, Vol. 13, 1976, pp. 1805–1816. doi:10.1103/PhysRevA.13.1805.

[45] Johnston, C. O., Brandis, A. M., , and Sutton, K., "Shock Layer Radiation Modeling and Uncertainty for Mars Entry," AIAA paper 2012-2866, 2012.

[46] Johnston, C. O., Mazaheri, A., Gnoffo, P., Kleb, B., and Bose, D., "Radiative Heating Uncertainty for Hyperbolic Earth Entry, Part 1: Flight Simulation Modeling and Uncertainty," *Journal of Spacecraft and Rockets*, Vol. 50, No. 1, 2013, pp. 19–38. doi:10.2514/1.A32254.

[47] Kulakhmetov, M., "Development of a Reduced C3 NEQAIR Radiation Model Based on Ab-Initio Calculations," Tech. rep., ARC-E-DAA-TN26173, 2015.

[48] Shinn, J. L., "Optical Absorption of Carbon and Hydrocarbon Species from Shock Heated Acetylene and Methane in the 135–220 nm Wavelength Range," AIAA paper 1981-1189, 1981.

[49] Arnold, J. O., Cooper, D. M., Park, C., and Prakash, S. G., "Line-by-Line Transport Calculations for Jupiter Entry Probes," AIAA paper 1979-1082, 1979.

[50] Cooper, D. M., and Jones, J. J., "An Experimental Determination of the Cross Section of the Swings Band System of C_3," *Journal of Quantitative Spectroscopy and Radiative Transfer*, Vol. 22, 1979, pp. 201–208.

[51] Prakash, S. G., and Park, C., "Shock Tube Spectroscopy of C_3+C_2H Mixture in the 140-700 nm Range," 1979.

[52] Brewer, L., and Engelke, J. L., "Spectrum of C_3," *Journal of Chemical Physics*, Vol. 36, No. 4, 1962, pp. 992–998.

[53] Gurvich, L. V., Veyts, I. V., and Alcock, C. B., *Thermodynamic Properties of Individual Substances*, Hemisphere Publishing Corp., New York, 1989.

[54] Jones, J. J., "The Optical Absorption of Triatomic Carbon C3 for the Wavelength Range 260 to 560 nm," Tech. rep., NASA TP-1141, 1978.

[55] Sharmai, M. P., Jaffe, R. L., Munafò, A., and Panesi, M., "Calculation of Thermochemical Properties of Carbon-cluster Ablation Species," AIAA paper 2018-4179, 2018. doi:10.2514/6.2018-4179.

[56] K, T. E., Dyakonov, A. A., Wright, M. J., and Tang, C. Y., "Aerothermodynamic Design of the Mars Science Laboratory Heatshield," AIAA paper 2009-4075, 2009.

Appendix

Table A1 Flowfield rate model.

#	Reaction	$A_{f,i}\left(\frac{cm^3}{mol-s}\right)$	$n_{f,i}$	$D_{f,i}(K)$	$T_{f,i}$	Third Body, M	Uncertainty Multiplier
	Dissociation Reactions						
1	C_2 + M ↔ 2C + M	4.500e+18	-1.00	7.1500e+04	T_a	All	0.1, 10.0
2	C_2H + M ↔ C_2 + H + M	1.700e+35	-5.16	5.7400e+04	T_a	All	0.1, 10.0
3	C_2H_2 + M ↔ C_2H + H + M	4.000e+16	0.00	5.4000e+04	T_a	All	0.1, 10.0
4	C_3 + M ↔ C_2 + C + M	1.680e+21	-1.50	8.7740e+04	T_a	H, C, N, O	0.1, 10.0
		8.400e+20	-1.50	8.7740e+04	T_a	others	0.1, 10.0
5	C_5 + M ↔ C_3 + C_2 + M	4.000e+14	0.00	8.1549e+04	T_{tr}	All	0.1, 10.0
6	CH + M ↔ C + H + M	1.900e+14	0.00	3.3717e+04	T_a	All	0.5, 2.0
7	CO + M ↔ C + O + M	1.800e+21	-1.00	1.2900e+05	T_a	H, C, N, O	0.25, 1.5
		1.200e+21	-1.00	1.2900e+05	T_a	others	0.25, 1.5
8	CO_2 + M ↔ CO + O + M	1.380e+22	-1.50	6.3275e+04	T_a	H, C, N, O	0.1, 1.0
		6.900e+21	-1.50	6.3275e+04	T_a	others	0.1, 1.0
9	H_2 + M ↔ 2H + M	8.500e+19	-1.10	5.2335e+04	T_a	H	0.1, 10.0
		9.000e+14	0.00	4.8400e+04	T_a	others	0.5, 2.0
10	O_2 + M ↔ 2O + M	1.000e+22	-1.50	5.9360e+04	T_a	H, C, O, N	0.5, 1.5
		2.000e+21	-1.50	5.9360e+04	T_a	others	0.5, 1.5
11	CH_2 + M ↔ C + H2 + M	1.300e+14	0.00	2.9700e+04	T_a	All	0.5, 2.0
12	CH_2 + M ↔ CH + H + M	4.000e+15	0.00	4.1800e+04	T_a	All	0.5, 2.0
13	He + M ↔ He^+ + e^- + M	1.330e+13	0.50	2.8516e+05	T_a	All	0.1, 10.0
	Exchange Reactions						
14	C_2 + C_2H_2 ↔ $2C_2H$	1.100e+14	-0.38	6.8700e+03	T_{tr}		0.1, 10.0
15	C_2H + H ↔ C_2 + H_2	1.600e+13	0.15	1.4600e+04	T_{tr}		0.1, 10.0
16	C_3 + C ↔ C_2 + C_2	6.000e+11	1.07	1.6500e+04	T_{tr}		0.1, 10.0
17	CH + C ↔ C_2 + H	2.000e+14	0.00	0.0000	T_{tr}		0.1, 10.0
18	CH + CO ↔ C_2H + O	2.500e+10	0.67	3.9000e+04	T_{tr}		0.1, 10.0
19	CO + C ↔ C_2 + O	2.000e+17	-1.00	5.8000e+04	T_{tr}		0.1, 10.0
20	CO + C_2 ↔ C_3 + O	1.000e+12	0.00	4.1200e+04	T_{tr}		0.1, 10.0
21	CO + O ↔ O_2 + C	3.900e+13	-0.18	6.9200e+04	T_{tr}		1.0, 10.0
22	CO_2 + O ↔ O_2 + CO	2.710e+14	0.00	3.3797e+04	T_{tr}		0.1, 10.0
23	H + C_2H_2 ↔ C_2H + H_2	1.000e+16	-0.50	1.5500e+04	T_{tr}		0.1, 10.0
24	H + CO ↔ CH + O	6.700e+14	0.15	8.8470e+04	T_{tr}		0.1, 10.0
25	H_2 + C ↔ CH + H	4.000e+14	0.00	1.1700e+04	T_{tr}		0.1, 10.0
26	CH_2 + H ↔ CH + H_2	6.030e+12	-0.00	-900	T_{tr}		0.1, 10.0
	Ionization Reactions						
27	C + e^- ↔ C^+ + e^- + e^-	3.900e+33	-3.78	1.3070e+05	T_{ve}		0.5, 10.0
28	H + e^- ↔ H^+ + e^- + e-	2.200e+30	-2.80	1.5780e+05	T_{ve}		0.05, 10.0
29	O + e^- ↔ O^+ + e^- + e^-	3.900e+33	-3.78	1.5850e+05	T_{ve}		0.1, 10.0

Table A2 Radiation mechanisms.

Species	Mechanism	Spectral range (eV)	Uncertainty
C	Lines	0-18	+/- 20%
	Photoionization	0-18	+/- 20%
H	Lines	0-18	+/- 1%
	Photoionization	0-18	+/- 20%
CO	4 + ($A^1\Pi - X^1\Sigma$)	6.0-10.0	+/- 40%
	3 + ($b^3\Sigma - a^3\Pi$)	3.0-5.0	+/- 50%
	$B^1\Sigma - X^1\Sigma+$	10.2-11.4	+/- 50%
	$C^1\Sigma - X^1\Sigma$	10.0-12.2	+/- 50%
	$E^1\Pi - X^1\Sigma$	11.2-11.9	+/- 50%
	Angstrom ($B^1\Sigma - A^1\Pi$)	0.5-3.2	+/- 50%
	Asundi ($a^3\Sigma - a^3\Pi$)	0.1-3.5	+/- 50%
	Triplet ($d^3\Delta - a^3\Pi$)	0.1-4.0	+/- 50%
	Infrared ($X^1\Sigma - X^1\Sigma$)	0.1-1.0	+/- 50%
C_2	Swan ($d^3\Pi_g - a^3\Pi_u$)	1.2-3.2	+/- 50%
	Ballik-Ramsay ($b^3\Sigma_g^- - a^3\Pi_u$)	0.4-2.5	+/- 50%
	Phillips ($A^1\Pi_u - X^1\Sigma_g^+$)	1.0-3.5	+/- 50%
	Mulliken ($D^1\Sigma_u^+ - X^1\Sigma_g^+$)	5.0-6.2	+/- 50%
	Des.-D'Azam. ($C^1\Pi_g - A^1\Pi_u$)	1.8-4.4	+/- 50%
	Fox-Herzberg ($e^3\Pi_g - a^3\Pi_u$)	2.5-6.2	+/- 50%
H_2	Lyman ($B^1\Sigma_u^+ - X^1\Sigma_g^+$)	10.0-14.0	+/- 10%
H_2	Werner ($C^1\Pi_u - X^1\Sigma_g^+$)	8.1-12.3	+/- 20%
C_3	Swings ($d^3\Pi_g - a^3\Pi_u$)	2.5-4.1	-1 om
	UV ( )	7.3-10.0	-1 om
C_2H	Continuum	4.6-6.5	+/- 1 om